Title	Quantifying the solid-fluid interfacial tensions depending on the substrate curvature: Young's equation holds for wetting around nanoscale cylinder
Author(s)	Watanabe, Keitaro; Kusudo, Hiroki; Bistafa, Carlos et al.
Citation	Journal of Chemical Physics. 2022, 156(5), p. 054701
Version Type	VoR
URL	https://hdl.handle.net/11094/97803
rights	Copyright 2022 Author(s). This article is distributed under a Creative Commons Attribution (CC BY) License.
Note	

The Journal of Chemical Physics

RESEARCH ARTICLE | FEBRUARY 01 2022

Quantifying the solid–fluid interfacial tensions depending on the substrate curvature: Young's equation holds for wetting around nanoscale cylinder

Keitaro Watanabe ; Hiroki Kusudo ; Carlos Bistafa ; Takeshi Omori ; Yasutaka Yamaguchi

J. Chem. Phys. 156, 054701 (2022)
https://doi.org/10.1063/5.0079816

AIP Publishing

The Journal of Chemical Physics | ARTICLE | scitation.org/journal/jcp

Quantifying the solid–fluid interfacial tensions depending on the substrate curvature: Young's equation holds for wetting around nanoscale cylinder

Cite as: J. Chem. Phys. **156**, 054701 (2022); doi: 10.1063/5.0079816
Submitted: 25 November 2021 • Accepted: 7 January 2022 •
Published Online: 1 February 2022

Keitaro Watanabe,[1,a)] Hiroki Kusudo,[1,b)] Carlos Bistafa,[1,c)] Takeshi Omori,[2,d)]
and Yasutaka Yamaguchi[1,3,e)]

AFFILIATIONS

[1] Department of Mechanical Engineering, Osaka University, 2-1 Yamadaoka, Suita 565-0871, Japan
[2] Deptartment of Mechanical Engineering, Osaka City University, 3-3-138 Sugimoto, Sumiyoshi, Osaka 558-8585, Japan
[3] Water Frontier Research Center (WaTUS), Research Institute for Science and Technology, Tokyo University of Science, 1-3 Kagurazaka, Shinjuku-ku, Tokyo 162-8601, Japan

[a)] **Present address:** Department of Management of Industry and Technology, Osaka University, Osaka 565-0871, Japan.
[b)] **Electronic mail:** hiroki@nnfm.mech.eng.osaka-u.ac.jp
[c)] **Electronic mail:** bistafa@nnfm.mech.eng.osaka-u.ac.jp
[d)] **Electronic mail:** omori@osaka-cu.ac.jp
[e)] **Author to whom correspondence should be addressed:** yamaguchi@mech.eng.osaka-u.ac.jp

ABSTRACT

By extending the theoretical framework derived in our previous study [Imaizumi *et al.*, J. Chem. Phys. **153**, 034701 (2020)], we successfully calculated the solid–liquid (SL) and solid–vapor (SV) interfacial tensions of a simple Lennard-Jones fluid around solid cylinders with nanometer-scale diameters from single equilibrium molecular dynamics systems in which a solid cylinder was vertically immersed into a liquid pool. The SL and SV interfacial tensions $\gamma_{SL} - \gamma_{S0}$ and $\gamma_{SV} - \gamma_{S0}$ relative to that for bare solid surface γ_{S0}, respectively, were obtained by simple force balance relations on fluid-containing control volumes set around the bottom and top ends of the solid cylinder, which are subject to the fluid stress and the force from the solid. The theoretical contact angle calculated by Young's equation using these interfacial tensions agreed well with the apparent contact angle estimated by the analytical solution to fit the meniscus shape, showing that Young's equation holds even for the menisci around solids with nanoscale curvature. We have also found that the curvature effect on the contact angle was surprisingly small while it was indeed large on the local forces exerted on the solid cylinder near the contact line. In addition, the present results showed that the curvature dependence of the SL and SV interfacial free energies, which are the interfacial tensions, is different from that of the corresponding interfacial potential energies.

I. INTRODUCTION

As we see cap-shaped liquid droplets on solid surfaces almost everyday, wetting behavior is one of the most common physical phenomena in human life and is also a research target in various scientific and engineering fields.[1–5] By defining the interfacial tensions and the contact angle θ, wetting is usually described by Young's equation[6]

$$\gamma_{SL} - \gamma_{SV} + \gamma_{LV} \cos\theta = 0, \tag{1}$$

where γ_{SL}, γ_{SV}, and γ_{LV} are solid–liquid (SL), solid–vapor (SV), and liquid–vapor (LV) interfacial tensions, respectively. Young's original idea of Eq. (1) in 1805 was the wall-tangential force balance of interfacial tensions exerted on the contact line (CL)—before the establishment of thermodynamics;[7] however, now, it is often explained from a thermodynamic point of view rather than from the mechanical balance.[1] Practically, the contact angle is used as a common measure of wettability. Various models have been proposed to capture the details of the CL, such as including the precursor film[1,8] or the microscopic contact angle[9] or considering the effects of line tension due to the contact-line curvature in Eq. (1).[10,11] However, it is difficult to experimentally validate these models mainly because measuring the interfacial tensions γ_{SL} and γ_{SV}, which include the solid surface, is also difficult.[12,13]

Wetting plays a key role in the nanoscale and from a microscopic theoretical point of view, Kirkwood and Buff[14] were the first to put forward the framework of surface tension based on the statistical mechanics. Recent development of molecular simulation methods including molecular dynamics (MD) and Monte Carlo (MC) advanced the microscopic understanding of the interfaces, and the calculation of the surface tension based on Bakker's equation,[2,3,15] which describes the relation between the stress integral through the liquid–vapor or liquid–gas interface and the surface tension, is used as a standard approach.[16] In addition, MD or MC studies about microscopic wetting have been conducted, ranging from simply evaluating the apparent contact angle, e.g., from the average droplet shape, to quantitatively extract the SL and SV interfacial tensions through a mechanical manner and/or a thermodynamic manner.[17–49] For the mechanical approach, called the mechanical route, Bakker's equation was extended to describe the connection between the stress integral through the SL or SV interface and the corresponding interfacial tension (see Appendix A).[23–29,49] On the other hand, for the latter approach, called the thermodynamic route, the SL and SV interfacial tensions were interpreted as the interfacial free energy per interfacial area. For instance, by the thermodynamic integration (TI) method, the SL interfacial energy was evaluated as the free energy difference from a reference system in which the SL interface was substituted by bare solid and liquid surfaces quasi-statically under constant number of particles N, temperature T, and pressure p (NpT-ensemble) or volume V (NVT-ensemble) condition.[27–36] These studies indicated that the apparent contact angle of the meniscus or droplet obtained in the simulations agreed well with the one predicted by Young's equation (1) in case the solid surfaces are flat and smooth so that the CL pinning may not be induced in a fully relaxed equilibrium state.[28] On the other hand, the force exerted from the solid on the fluid should be included in Young's equation in case the contact line is pinned due to a chemical inhomogeneity of the solid.[29]

Considering the potential applications of nano-wetting, e.g., a flow in a confined space such as a nanofoam[50] or a carbon nanotube (CNT),[51] the solid surfaces can have a nanoscale radius of curvature, and the interfacial tensions should depend on the curvature. Regarding the water wetting on carbon nanotubes as a solid with a nanoscale curvature, unique wetting behavior[52] and a strong diameter dependence of the capillary force were experimentally reported.[53] For the liquid–vapor interface, Tolman[54] first formulated the size effect of droplet surface tension with a lengthscale called the "Tolman length,"[55–57] and MD or MC simulations have been carried out as well.[38,58–62] Indeed, the LV interfacial tension can be extracted using a strict definition of the interface position, e.g., based on the force and momentum balances[58] and the difference between the pressures inside and outside the droplet based on the Young–Laplace equation. On the other hand, the calculation of the SL and SV interfacial tension on a curved solid surface is not trivial.[60,63] For instance, via thermodynamic routes, if we suppose calculation systems for the TI to calculate the SL interfacial tension on a cylindrical solid surface with a nanoscale radius, then, the three interface areas, i.e., the radii of the target solid–fluid (SF) , the reference bare solid, and bare liquid interfaces, should be all different, and this difference would become critical for the evaluation of the desired interfacial tension when the cylinder radius is comparable to the radius differences. Another possibility is via mechanical routes, and it is technically possible to calculate the stress distribution in the cylindrical or spherical coordinates, although the calculation cost significantly increases to obtain the distribution, and indeed, precise calculation in these coordinate systems is not implemented into the MD packages such as LAMMPS[64] or GROMACS,[65] and the implementation into in-house codes is also rather complicated.[58,66]

Going back to the relation between the SL or SV interfacial tension and the fluid stress in the interface via the mechanical routes, what we need is not the stress distribution but the stress integral. Considering this feature, in our previous study,[26] we provided a theoretical framework to extract the SL and SV interfacial tensions from a single MD simulation by using the local forces and the local interaction potential exerted on a quasi-two-dimensional (2D) flat and smooth solid plate immersed into a liquid pool of a simple liquid, called the Wilhelmy plate, and verified through the comparison between the MD results and the interfacial works of adhesion obtained by the TI. This modified Wilhelmy method is advantageous because it does not require computationally demanding calculations such as the local stress distributions and the thermodynamic integration, which needs averaging at each discrete states along the integration path.

In this study, we extracted the SL and SV interfacial tensions of a simple Lennard-Jones (LJ) fluid around solid cylinders with nanometer-scale radii by applying the modified Wilhelmy equations derived in our previous study[26] to investigate the curvature effect[67] on the SL and SV interfacial tensions. From the results, we also examined whether Young's equation holds even for menisci around solids with nanoscale curvature. Finally, we discuss the difference in the curvature dependence between the SL and SV interfacial tensions (free energy) and the SL and SV interaction potential energies (part of the internal energy).

II. METHOD

In this study, we employed equilibrium MD simulation systems of a quasi-axisymmetric meniscus on a hollow closed cylinder dipped into a liquid pool of a simple fluid as shown in Fig. 1. All the simulations were carried out by using our in-house code. Except the boundary condition in the lateral directions, the basic setup is similar to our previous study of the quasi-2D meniscus formed on a hollow rectangular solid plate.[26] Generic particles modeled by a LJ potential were used as the fluid particles. The 12-6 LJ potential given by

$$\Phi^{\mathrm{LJ}}(r_{ij}) = 4\epsilon\left[\left(\frac{\sigma}{r_{ij}}\right)^{12} - \left(\frac{\sigma}{r_{ij}}\right)^{6} + c_2^{\mathrm{LJ}}\left(\frac{r_{ij}}{r_{\mathrm{c}}}\right)^{2} + c_0^{\mathrm{LJ}}\right] \tag{2}$$

was applied for the interaction between fluid particles, where r_{ij} denotes the distance between the particles i at position $\boldsymbol{r}_i$ and j at $\boldsymbol{r}_j$ while ϵ and σ are the LJ energy and length parameters, respectively. This LJ interaction was truncated at a cutoff distance of $r_c = 3.5\sigma$, where quadratic functions were added so that the potential and interaction force smoothly became zero at r_c. The constant values c_2^{LJ} and c_0^{LJ} were given in our previous study.[25] Hereafter, fluid and solid particles are expressed by "f" and "s," respectively, and corresponding combinations are denoted by subscripts. Most of the simulation parameters are the same as in our previous study, and the values are summarized in Table I with the non-dimensional units normalized by the corresponding standard values based on ϵ_{ff}, σ_{ff}, and m_{f}.

Three solid cylinders in contact with the fluid were prepared by using the geometrical configuration of single-walled carbon nanotubes (CNTs) with their chiral indices of (20,0), (40,0), and (80,0), where the solid particles were fixed on the coordinate with the positions of the hexagonal periodic structure with an inter-particle distance r_{ss} of 0.141 nm, i.e., the immobile solid particles formed a hollow single-layered solid surface. Note that the present homogeneous solid surface is considered to be smooth with r_{ss} much smaller than σ_{ff} and σ_{sf}, and the CL is quickly relaxed without hysteresis effects on this surface, i.e., pinning is not induced on this surface. The corresponding radii R_{s} of the cylinder are 0.777, 1.55, and 3.11 nm, respectively. The central axis of the cylinders is set on the z axis, i.e., the zigzag edge of the honeycomb structure was set parallel to the xy-plane. The top and bottom parts of the cylinders are covered by locating additional solid particles as the lid to prevent fluid particles from entering into the cylinder. Note that the structure of these lids does not have direct effect on the simulation results as indicated in our previous study.[26]

The solid–fluid interaction, which expresses the SL or SV interaction, was also modeled by the LJ potential in Eq. (2), where the length parameter σ_{sf} was determined by the Lorentz mixing rule, whereas the energy parameter ϵ_{sf} was varied in a parametric manner by multiplying a SF interaction coefficient η to the base value given by the Berthelot rule $\epsilon_{\mathrm{sf}}^0 = \sqrt{\epsilon_{\mathrm{ff}}\epsilon_{\mathrm{ss}}}$ as

$$\epsilon_{\mathrm{sf}} = \eta\epsilon_{\mathrm{sf}}^0. \tag{3}$$

Wettability was expressed by this parameter η, i.e., the contact angle of a hemi-cylindrically shaped equilibrium droplet on a homogeneous flat solid surface and η had a one-to-one correspondence,[25,28,29] and we set the parameter η between 0.03 and 0.15 so that the corresponding cosine of the contact angle $\cos\theta$ is from −0.9 to 0.9. The definition of the contact angle is shown later in Sec. III. Note that since the solid–solid inter-particle distance r_{ss} was relatively small compared to the LJ length parameters σ_{ff} and σ_{fs}, the surface is considered to be very smooth, and the wall-tangential force acting from the solid on the fluid, which induces pinning of the CL, is negligible within the framework such that the stress is defined only by the fluid–fluid interaction and fluid motion, and solid force is dealt with as the external force.[28,29,68] Note that this condition can be violated for wetting on a soft solid.[45]

We set a horizontal potential wall on the bottom (floor) of the calculation cell fixed at $z = z_{\mathrm{flr}}$ about 5.3 nm below the bottom of the solid plate, which interacted only with the fluid particles with a one-dimensional potential field $\Phi_{\mathrm{flr}}^{\mathrm{1D}}$ as the function of the distance from the wall given by

$$\Phi_{\mathrm{flr}}^{\mathrm{1D}}(z_i') = 4\pi\rho_{\mathrm{n}}\epsilon_{\mathrm{sf}}^{\mathrm{flr}}\sigma_{\mathrm{sf}}^2\left[\frac{1}{5}\left(\frac{\sigma_{\mathrm{sf}}}{z_i'}\right)^{10} - \frac{1}{2}\left(\frac{\sigma_{\mathrm{sf}}}{z_i'}\right)^{4} + c_2^{\mathrm{flr}}\left(\frac{z_i'}{z_{\mathrm{c}}^{\mathrm{flr}}}\right)^2 + c_1^{\mathrm{flr}}\left(\frac{z_i'}{z_{\mathrm{c}}^{\mathrm{flr}}}\right) + c_0^{\mathrm{flr}}\right], \tag{4}$$

$$z_i' \equiv z_i - z_{\mathrm{flr}}, \tag{5}$$

where z_i is the z-position of the fluid particle i and $\epsilon_{\mathrm{sf}}^{\mathrm{flr}}$ is set at $0.09\epsilon_{\mathrm{sf}}^0$. This potential wall equivalently expressed a mean potential field formed by a single layer of solid particles with a constant area number density ρ_{n}. Similar to Eq. (2), this potential field in Eq. (4) was at a distance of $z_{\mathrm{c}}^{\mathrm{flr}} = 3.5\sigma_{\mathrm{sf}}$, and a quadratic function was added for a smooth truncation at $z_{\mathrm{c}}^{\mathrm{flr}}$. As shown in Fig. 1, fluid particles were rather strongly adsorbed onto this plane because this roughly corresponded to a completely wetting solid wall. With this setup, the liquid pool was stably maintained even in case the liquid pressure is low with a highly wettable solid cylinder or a plate, and a sufficient liquid bulk region was kept between this wall and the bottom of the cylinder or the plate. Furthermore, we set another horizontal potential wall on the top (ceiling) of the calculation cell fixed at $z = z_{\mathrm{ceil}}$ about 4.7 nm above the top of the cylinder or the plate exerting a repulsive potential field $\Phi_{\mathrm{ceil}}^{\mathrm{1D}}$ on the fluid particles expressed by

$$\Phi_{\mathrm{ceil}}^{\mathrm{1D}}(z_i'') = 4\pi\rho_{\mathrm{n}}\epsilon_{\mathrm{sf}}^{\mathrm{ceil}}\sigma_{\mathrm{sf}}^2\left[\frac{1}{5}\left(\frac{\sigma_{\mathrm{sf}}}{z_i''}\right)^{10} + c_2^{\mathrm{ceil}}\left(\frac{z_i''}{z_{\mathrm{c}}^{\mathrm{ceil}}}\right)^2 + c_1^{\mathrm{ceil}}\left(\frac{z_i''}{z_{\mathrm{c}}^{\mathrm{ceil}}}\right) + c_0^{\mathrm{ceil}}\right], \tag{6}$$

$$z_i'' \equiv z_{\mathrm{ceil}} - z_i, \tag{7}$$

TABLE I. Simulation parameters and their corresponding non-dimensional values.

Property	Value	Unit	Non-dim. value
σ_{ff}	0.340	nm	1
σ_{sf}	0.357	nm	1.05
r_{ss}	0.141	nm	0.415
ϵ_{ff}	1.67×10^{-21}	J	1
ϵ_{sf}^0	1.96×10^{-21}	J	1.18
$\epsilon_{\mathrm{sf}}^{\mathrm{flr}}$	0.176×10^{-21}	J	0.106
$\epsilon_{\mathrm{sf}}^{\mathrm{ceil}}$	0.176×10^{-21}	J	0.106
$\epsilon_{\mathrm{sf}}^{\mathrm{sid}}$	0.192×10^{-21}	J	0.115
ϵ_{sf}	$\eta \times \epsilon_{\mathrm{sf}}^0$		
η	0.03–0.15	⋯	⋯
m_{f}	6.64×10^{-26}	kg	1
R_{s}	0.777–3.11	nm	2.29–9.15
R_{sid}	9	nm	26.5
T	90	K	0.703
N_{f}	53 778–60 834	⋯	⋯

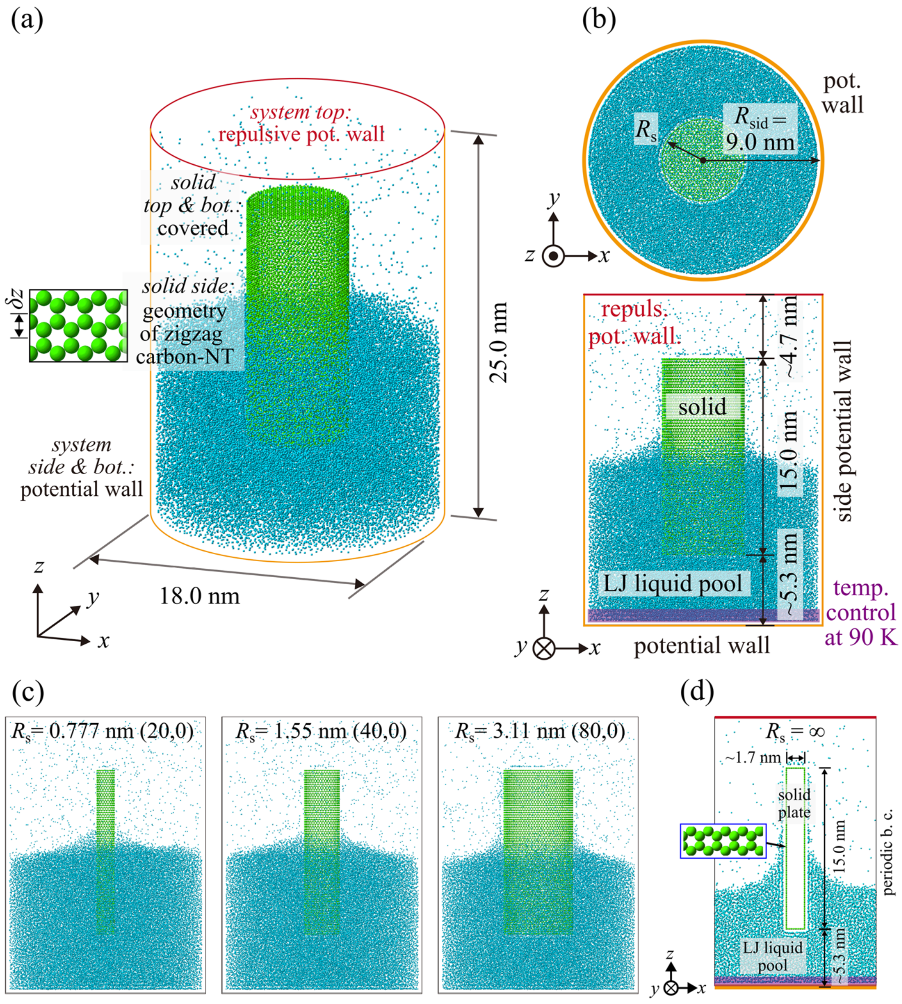

FIG. 1. (a) A bird-eye view and (b) top and (c) side views of equilibrium molecular dynamics (MD) simulation systems of hollow solid cylinders dipped into a liquid pool of a simple Lennard-Jones (LJ) fluid. (d) Side view of the system with a hollow solid plate (see Ref. 26 for details).

where $\epsilon_{\rm sf}^{\rm ceil}$ is identical to $\epsilon_{\rm sf}^{\rm flr}$ while a cutoff distance of $z_{\rm c}^{\rm ceil} = \sigma_{\rm sf}$ is used to achieve a repulsive potential field.

In addition to these bottom and top potential walls, we also set another cylindrical side potential wall with its axis on the z axis and with a radius $R_{\rm sid}$, which exerts a one-dimensional potential field on the fluid particles $\Phi_{\rm sid}^{\rm 1D}(r_i^{xy})$ as the function of the horizontal distance from the wall given by

$$\Phi_{\rm sid}^{\rm 1D}(r_i^{xy}) = 4\pi\rho_{\rm n}\epsilon_{\rm sf}^{\rm sid}\sigma_{\rm sf}^2\left[\frac{1}{5}\left(\frac{\sigma_{\rm sf}}{r_i^{xy}}\right)^{10} - \frac{1}{2}\left(\frac{\sigma_{\rm sf}}{r_i^{xy}}\right)^{4} + c_2^{\rm flr}\left(\frac{r_i^{xy}}{r_{\rm c}^{\rm sid}}\right)^{2} + c_1^{\rm flr}\left(\frac{r_i^{xy}}{r_{\rm c}^{\rm sid}}\right) + c_0^{\rm sid}\right], \tag{8}$$

$$r_i^{xy} \equiv R_{\rm sid} - \sqrt{x_i^2 + y_i^2}, \tag{9}$$

where r_i^{xy} is the lateral distance of the fluid particle i from the side potential wall. Note that this side wall was adopted to achieve a quasi-axisymmetric 2D-meniscus instead of applying the periodic boundary condition in the horizontal x- and y-directions as in our previous study with a solid plate. The parameter $\epsilon_{\rm sf}^{\rm sid}$ was set at $0.0975\epsilon_{\rm sf}^{0}$ so that the resulting contact angle at the side wall may be roughly 90°. The radius $R_{\rm sid}$ was chosen so that a sufficiently large LV interface could be kept, excluding the adsorption layers on the solid cylinder and on the side wall. With this condition, we assumed that the LV interfacial tension $\gamma_{\rm LV}$ was constant there, and we evaluated the apparent contact angle from the differential equation for the shape of an axisymmetric meniscus there as described below with Fig. 2.

The system was kept at a constant temperature T of 90 K, which is above the triple point temperature,[69] by applying velocity rescaling to the fluid particles within 0.8 nm from the floor potential wall only for the velocity components in the x- and y-directions. This thermostat region was sufficiently away from the bottom of the solid cylinder/plate, and no direct thermostating was applied to the region near the solid so that this thermostat had no effects on the present results.

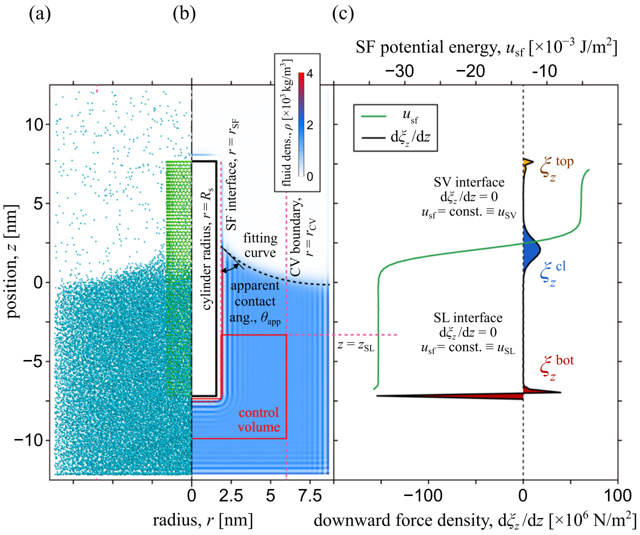

FIG. 2. (a) Half side snapshot, (b) distribution of the time-averaged fluid density, and (c) distributions of the time-averaged downward force density acting on the solid plate and solid–fluid (SF) potential energy density per solid surface area for the system with the solid radius R_s = 1.55 nm and a SF interaction parameter η = 0.15.

With this setting, an axisymmetric quasi-2D LJ liquid with a meniscus-shaped LV interface and the CL parallel to the xy-plane was formed as an equilibrium state as exemplified in Fig. 1, where a liquid bulk with an isotropic density was formed above the bottom wall by choosing a proper number of fluid particles N_f as shown in Fig. 2. We verified that the temperature was constant in the whole system after the equilibration run described in the following. The velocity Verlet method was used for the integration of the Newtonian equation of motion with a time increment of 5 fs for all systems.

We obtained the physical properties of each equilibrium system with various cylinder radii R_s and η values as the time average of 20 ns, which followed an equilibration run of more than 10 ns.

III. RESULTS AND DISCUSSION

A. Apparent contact angle

Similar to our previous study,[26] we obtained the distribution of force acting from the fluid on the solid particles by dividing the solid region into equal-sized bins in the z-direction, where a bin height of δz = 0.2115 nm was used, considering the periodicity of the CNT structure. The average force density $d\xi_z/dz$ was defined by the time-averaged total downward (in $-z$-direction) force from the fluid on the solid particles in each bin divided by the solid bin area $2\pi R_s \delta z$. Except at the top and bottom of the cylinder or the plate, $d\xi_z/dz$ expresses the downward force per surface area. The average SF potential energy per area u_{sf} was also calculated, which was obtained by substituting the downward force by the SF potential energy.

A half side snapshot and the distribution of time-averaged fluid density ρ around the solid cylinder are shown for the system with SF interaction parameter η = 0.15 in Fig. 2. The time-averaged distributions of the downward force exerted on the solid cylinder $d\xi_z/dz$ and the SF potential energy u_{sf} are also shown in the right panel. We briefly summarize two essential features in the following, which are qualitatively the same as in our previous study.[26] (1) Multi-layered adsorption layers were formed around the solid cylinder and the bottom and side potential walls, and liquid bulk with a homogeneous density is observed away from the cylinder, potential walls, and the LV interface. (2) The total downward force as the integral of $d\xi_z/dz$ can be clearly separated into three local parts, i.e., ξ_z^{top} around the top, ξ_z^{cl} around the contact line, and ξ_z^{bot} around the bottom. As indicated in Fig. 2(c), ξ_z^{top} and ξ_z^{cl} are positive, i.e., downward forces were exerted, and ξ_z^{bot} is negative, i.e., an upward force was exerted. As in our previous study, the distributions of $d\xi_z/dz$ and u_{sf} around the top and bottom had less physical meaning because the top and bottom solid lids in the bin were included, and these parts for u_{sf} are not shown in the figure. However, the local integral of $d\xi_z/dz$ had the physical information about the force around the top and bottom parts. Note that ξ_z has the dimension of force per length, which is the same as the surface tension.

As exemplified in the density distribution in Fig. 2(b), we evaluated the contact angles for the plate and cylinder systems with different SF interaction parameters to examine the curvature effects. For the plate system, we followed the same procedure used to determine the apparent contact angle as our previous study:[26] the LV interface was defined as the least-squares fitting circle on the density contour of ρ = 400 kg/m^3 at the LV interface at height $z(x)$ excluding the region in the adsorption layers near the solid.[25,26,28,29] For the cylinder systems, the contact angles were evaluated using the analytical formula of the macroscopic meniscus shape. For an axisymmetric equilibrium meniscus around a z-centered cylinder with neglecting gravity, it follows for the meniscus height $z(r)$ given as a unique function of the radial position $r \equiv \sqrt{x^2 + y^2}$ that

$$\frac{1}{r}\frac{d}{dr}[r \sin \psi(r)] = \frac{p_V^{blk} - p_L^{blk}}{\gamma_{LV}}, \quad \tan \psi(r) = \frac{dz(r)}{dr}, \tag{10}$$

where $\psi(r)$ denotes the angle from the r-direction. We evaluated the three constant values in this differential equation (10) from MD simulations: γ_{LV} was obtained from a MD system with planer LV interfaces by a standard mechanical process,[27] whereas p_V^{blk} and p_L^{blk} were evaluated as the force per area on the top and bottom potential walls of the present cylinder system, respectively, both excluding the region near the side wall. Thus, by fitting the density contour of ρ = 400 kg/m^3 at the LV interface excluding the region in the adsorption layers formed near the solid surface and also excluding that near the side potential wall, a numerical solution of the 2nd-order ordinary differential equation (10) can be obtained for each system with different cylinder radii R_s and SF interaction parameters η. As shown by the dotted black line in Fig. 2, the meniscus shape is well reproduced in this system. We determined the contact angle as the angle between the extrapolated solution of the meniscus shape and the SF-interface position in the rz-plane including the liquid side.

We also considered a concave control volume (CV) shown in red color in Fig. 2(b) around the bottom of the cylinder to calculate the SL interfacial tension below. The bottom face and the side cylindrical face of the CV are in the liquid bulk, where the former is sufficiently away from both the bottom of the system and bottom of the cylinder, whereas the latter at $r = r_{\rm CV}$ is away from the side boundary. Analogously, the top face is at the height $z = z_{\rm SL}$ sufficiently away from both the bottom of the cylinder and the contact line. On the other hand, the concave faces are set at the SL boundary with its inner side face at $r = r_{\rm SF}$.

The density distributions around the solid cylinder with the smallest radius $R_{\rm s} = 0.777$ nm and the plate and the relation between the SF interaction coefficient η and cosine of the contact angle $\cos\theta_{\rm app}$ are shown in Fig. 3. For the latter, we displayed the error bars and guide lines only for the plate and for the cylinder systems with $R_{\rm s} = 0.777$ nm for better visualization: the error bars for the systems with other radii were comparable to those for $R_{\rm s} = 0.777$ nm. As shown in Fig. 3(a), the apparent meniscus shapes of the cylinder and plate are different, indicating that different force balances should be adopted to properly evaluate the contact angle from the meniscus shape. With the increase of η, the solid became more wettable, i.e., $\cos\theta_{\rm app}$ increased, and the cylinder with the smallest radius $R_{\rm s} = 0.777$ nm was less wettable, i.e., had smaller $\cos\theta_{\rm app}$ than the plate for all η values tested. However; we should stress that the radius dependence of the contact angle shown in Fig. 3(b) was unexpectedly small even with the smallest cylinder with its radius $R_{\rm s}$ that is comparable to $\sigma_{\rm ff}$ or $\sigma_{\rm sf}$. We discuss the reason in the following with the comparison between the apparent contact angle $\theta_{\rm app}$ and the contact angle predicted by Young's equation (1) using the interfacial tensions obtained by the local forces.

B. Curvature dependence of the force around the contact line and the solid–liquid and solid–vapor interfacial tensions

We further investigate the curvature dependence of wetting behavior with the calculations of $\xi_z^{\rm cl}$ and the interfacial tensions. We start from the extraction of the upward force $F_z^{\rm bot}$ exerted from the solid on the liquid in the red control volume (CV) around the bottom illustrated in the top-left panel of Fig. 4. Note that we evaluate the upward force F_z on the corresponding liquid from the solid as follows: the positive direction for F_z is $+z$-direction and is opposite to that for ξ_z (force per length) in the $-z$-direction on the corresponding solid from the liquid. The top face of the CV at $z = z_{\rm SL}$ is sufficiently away from both the bottom of the solid and the contact line, where the liquid density ρ near the solid is constant in the z-direction, satisfying

$$\frac{\partial \rho}{\partial z} = 0 \quad \text{for} \quad (r - R_{\rm s})^2 + (z - z_{\rm SL})^2 \le (r_{\rm c}^{\rm sf})^2 \tag{11}$$

with $r_{\rm c}^{\rm sf}$ the cutoff distance for SF interaction. The force of present interest $F_z^{\rm bot}$ comes from the neighboring solid within the cutoff range, i.e., from the red-dotted and black-dotted solid parts as indicated by the blue arrows (top-left panel). On the other hand, with the condition in Eq. (11), the sum of the upward forces on the liquid parts in the red-solid and black-solid lines from the red-dotted solid part (bottom-left panel) is $2\pi R_{\rm s}\xi_z^{\rm bot}$, which is the reaction force on the solid around the bottom indicated in Fig. 2. From the comparison of the arrows regarding the two, $F_z^{\rm bot}$ is obtained by adding the missing force and subtracting the unnecessary force as in the bottom panel as

$$\begin{aligned} F_z^{\rm bot} &= 2\pi R_{\rm s}\xi_z^{\rm bot} + F_z^{\rm diag(SL)} - \left(-F_z^{\rm diag(SL)}\right) \\ &= 2\pi R_{\rm s}\xi_z^{\rm bot} + 2F_z^{\rm diag(SL)}, \end{aligned} \tag{12}$$

where the two "diagonal" forces denoted by $F_z^{\rm diag(SL)}$ and $-F_z^{\rm diag(SL)}$ have an opposite sign with the same absolute value due to the symmetry under the condition in Eq. (11).

The value of unknown $F_z^{\rm diag(SL)}$ now must be determined. Although this $F_z^{\rm diag(SL)}$ can be obtained directly by MD simulations based on the definition, in the special case where the solid is so smooth compared to the lengthscale of SF inter-particle interaction that the density can be considered a constant independent of the position as the present solid with the graphene geometry, $F_z^{\rm diag(SL)}$ can be analytically expressed by

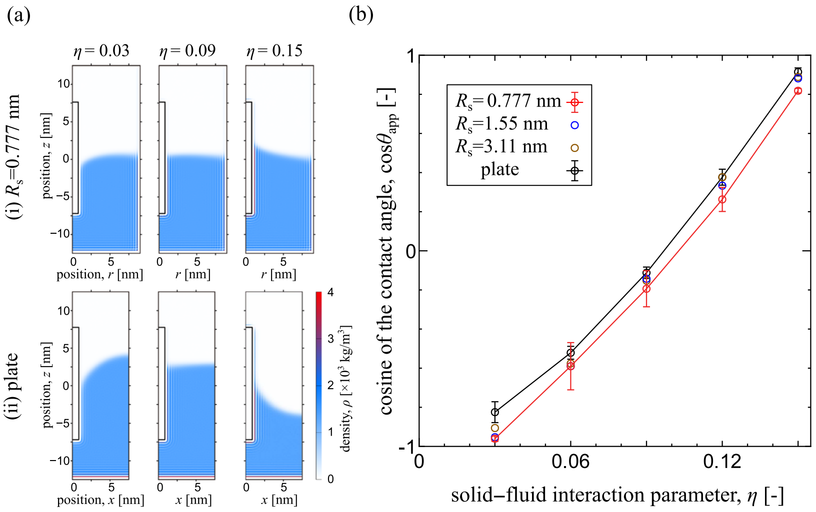

FIG. 3. (a) Density distributions around the (i) solid cylinder of radius $R_{\rm s}$ = 0.777 nm and (ii) plate and (b) relation between the cosine of the contact angle and solid–fluid interaction parameter for different cylinder radii $R_{\rm s}$ and the plate.

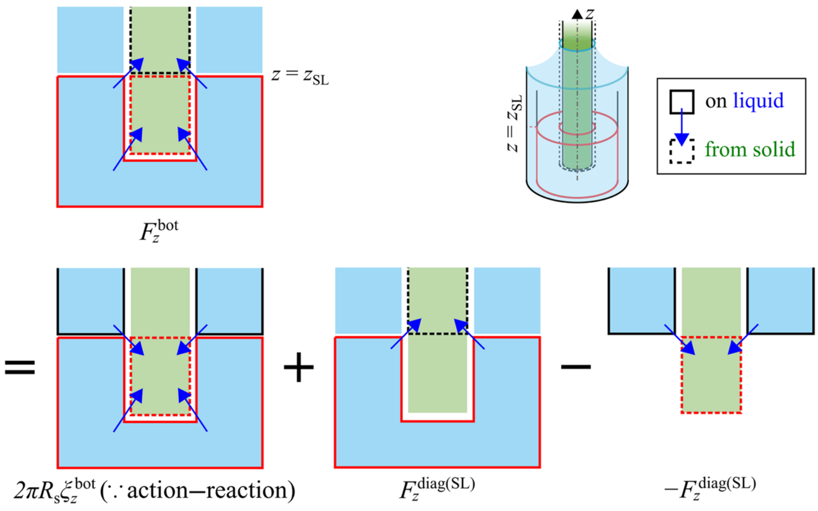

FIG. 4. Schematic of the extraction of the *z*-direction force from the solid on the fluid in the red control volume around the bottom, considering the force distribution in Fig. 2.

$$F_z^{\rm diag(SL)} = -\pi R_s u_{\rm SL}. \tag{13}$$

The detailed derivation is described in Appendix B. Similarly, the diagonal force $F_z^{\rm diag(SV)}$ on the vapor below a plane $z = z_{\rm SV}$ from the solid above the plane can also be analytically formulated by

$$F_z^{\rm diag(SV)} = -\pi R_s u_{\rm SV}. \tag{14}$$

By considering a force balance similar to that illustrated in Fig. 4 and by also assuming that the solid is smooth and the fluid particles are not pinned around the contact line, the downward force on the solid $\xi_z^{\rm cl}$ per length is analytically given by (see Appendix C for details)

$$\xi_z^{\rm cl} = -u_{\rm SL} + u_{\rm SV} = (-u_{\rm SL}) - (-u_{\rm SV}), \tag{15}$$

where the final equality shows that $\xi_z^{\rm cl}$ is the difference in the magnitude between the two interfacial potential energy densities, considering that $u_{\rm SL}$ and $u_{\rm SV}$ are both negative as exemplified in Fig. 2.

Figure 5 shows the dependence of SL and SV potential energy densities $-u_{\rm SL}$ and $-u_{\rm SV}$ on the SF interaction parameter η for solid plate and solid cylinders with different radii R_s and the comparison between the downward force $\xi_z^{\rm cl}$ on the solid around the CL and the difference of potential energy density $-u_{\rm SL} + u_{\rm SV}$. As easily expected, $-u_{\rm SL}$ and $-u_{\rm SV}$ increased with the increase of η as shown in the left panel; however, $-u_{\rm SL}$ and $-u_{\rm SV}$ showed opposite dependence on R_s: $-u_{\rm SL}$ was larger for the smaller cylinder radius R_s whereas $-u_{\rm SV}$ was smaller. We will discuss this interesting difference later. In the right panel of Fig. 5, a very good agreement between $\xi_z^{\rm cl}$ and $-u_{\rm SL} + u_{\rm SV}$ is observed for the whole range of η with different radii R_s. This indicates that the force from the solid on the liquid in the CV around the bottom shown as a red concave in Fig. 4 can be properly evaluated by Eq. (13) because the present system with solid particles located at the position of graphene was supposed to be sufficiently smooth to meet the condition assumed in the analytical derivation in Appendixes B and C. In addition, due to the opposite radius dependence of $-u_{\rm SL}$ and $-u_{\rm SV}$ shown in the left panel, the difference of $\xi_z^{\rm cl}$ for the smallest radius and that for the plate was as large as about 10×10^{-3} N/m,

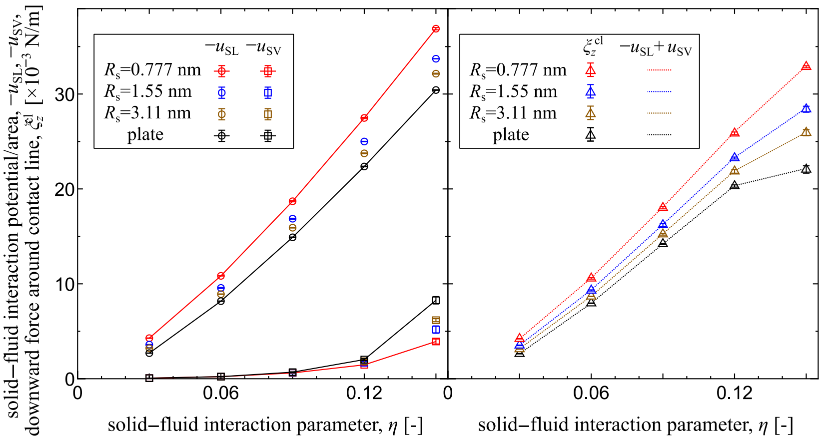

FIG. 5. (Left) dependence of SL and SV potential energy densities $-u_{\rm SL}$ and $-u_{\rm SV}$ on the solid–fluid interaction parameter η for solid plate and solid cylinders with different radii R_s. (Right) comparison between the downward force $\xi_z^{\rm cl}$ on the solid around the CL and the difference of the potential energy density $-u_{\rm SL} + u_{\rm SV}$.

which is comparable to γ_{LV}. In addition, ξ_z^{cl} was much larger than the difference of $-(\gamma_{\mathrm{SL}} - \gamma_{\mathrm{S0}})$ and $-(\gamma_{\mathrm{SV}} - \gamma_{\mathrm{S0}})$ shown later.

We now examine the relative SL interfacial tension by using the total static force balance including the force F_z^{bot} on the red-solid CV in Fig. 4,

$$2\pi \int_{r_{\mathrm{SF}}}^{r_{\mathrm{CV}}} \mathrm{d}r\, \tau_{zz}(r, z_{\mathrm{SL}}) r + \pi r_{\mathrm{CV}}^2 p_{\mathrm{L}}^{\mathrm{blk}} + F_z^{\mathrm{bot}} = 0, \tag{16}$$

where the first and second terms of the LHS are the fluid stress integral on the top face and pressure from the bottom, respectively. Note that the side boundary is set at the bulk satisfying $\tau_{rz} = 0$ and also that the fluid stress is zero on the faces around the concave under the present stress definition.[3,26,28,68] The first term of the LHS is related to the relative SL interfacial tension $\gamma_{\mathrm{SL}} - \gamma_{\mathrm{S0}}$ with extended Bakker's equation applied for a cylindrical SL interface by (see Appendix A)

$$\gamma_{\mathrm{SL}} - \gamma_{\mathrm{S0}} = \frac{1}{r_{\mathrm{SF}}}\left[\int_{r_{\mathrm{SF}}}^{r_{\mathrm{CV}}} \mathrm{d}r\, \tau_{zz}(r, z_{\mathrm{SL}}) r + \frac{(r_{\mathrm{CV}}^2 - r_{\mathrm{SF}}^2) p_{\mathrm{L}}^{\mathrm{blk}}}{2}\right]. \tag{17}$$

Thus, from Eqs. (12), (16), and (17), $\gamma_{\mathrm{SL}} - \gamma_{\mathrm{S0}}$ results in

$$\gamma_{\mathrm{SL}} - \gamma_{\mathrm{S0}} = -\frac{R_{\mathrm{s}}}{r_{\mathrm{SF}}} \xi_z^{\mathrm{bot}} - \frac{r_{\mathrm{SF}}}{2} p_{\mathrm{L}}^{\mathrm{blk}} - \frac{F_z^{\mathrm{diag(SL)}}}{\pi r_{\mathrm{SF}}}, \tag{18}$$

where the pressure $p_{\mathrm{L}}^{\mathrm{blk}}$ was measured in MD systems as the normal force per area exerted on the bottom potential wall for $r \le r_{\mathrm{CV}}$ because this external force balances the constant bulk wall-normal pressure.[28] Under the condition that Eq. (13) holds for $F_z^{\mathrm{diag(SL)}}$ as in the present systems, Eq. (12) is further rewritten by

$$F_z^{\mathrm{bot}} = 2\pi R_{\mathrm{s}} \left(\xi_z^{\mathrm{bot}} - u_{\mathrm{SL}}\right), \tag{19}$$

and Eq. (18) writes

$$\gamma_{\mathrm{SL}} - \gamma_{\mathrm{S0}} = -\frac{R_{\mathrm{s}}}{r_{\mathrm{SF}}} \xi_z^{\mathrm{bot}} - \frac{r_{\mathrm{SF}}}{2} p_{\mathrm{L}}^{\mathrm{blk}} + \frac{R_{\mathrm{s}}}{r_{\mathrm{SF}}} u_{\mathrm{SL}}. \tag{20}$$

Similarly, the relative solid–vapor interfacial tension $\gamma_{\mathrm{SV}} - \gamma_{\mathrm{S0}}$ writes

$$\gamma_{\mathrm{SV}} - \gamma_{\mathrm{S0}} = \frac{R_{\mathrm{s}}}{r_{\mathrm{SF}}} \xi_z^{\mathrm{top}} - \frac{r_{\mathrm{SF}}}{2} p_{\mathrm{V}}^{\mathrm{blk}} + \frac{R_{\mathrm{s}}}{r_{\mathrm{SF}}} u_{\mathrm{SV}}. \tag{21}$$

Note that Eqs. (20) and (21) are equivalent to the derivation for the quasi-2D Wilhelmy plate[26] except the point that the radii of the solid surface area R_{s} and solid–fluid interface area r_{SF} are different for the present Wilhelmy-cylinders. In addition, note that the meniscus shape including the contact angle does not explicitly appear in Eqs. (20) and (21).

Figure 6 shows the relative SL and SV interfacial tensions calculated by Eqs. (20) and (21) for different solid radii R_{s} with various wettability parameters η. For a direct comparison between the two interfacial tensions, the values $-(\gamma_{\mathrm{SL}} - \gamma_{\mathrm{S0}}) + \gamma_{\mathrm{LV}}$ and $-(\gamma_{\mathrm{SV}} - \gamma_{\mathrm{S0}})$ are shown with the left vertical axis, which correspond to the works of adhesion

$$W_{\mathrm{SL}} \equiv -(\gamma_{\mathrm{SL}} - \gamma_{\mathrm{S0}}) + \gamma_{\mathrm{LV}} \tag{22}$$

and

$$W_{\mathrm{SV}} \equiv -(\gamma_{\mathrm{SV}} - \gamma_{\mathrm{S0}}), \tag{23}$$

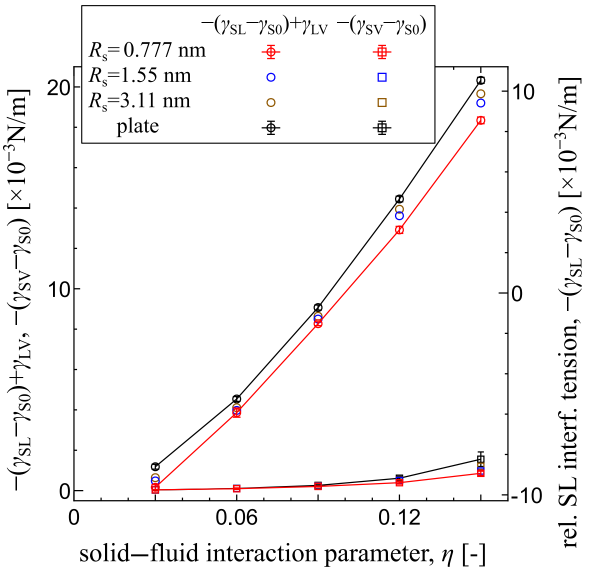

FIG. 6. Dependence of the SL and SV interfacial tensions on the radius of solid cylinders with different wettabilities.

where the value of $\gamma_{\mathrm{LV}} = 9.79 \times 10^{-3}$ N/m obtained in our previous study[26] was used. For a flat interface, they are defined as the minimum works needed to strip the liquid and vapor off the flat solid surface, respectively, under the constant temperature and pressure condition.[28,36] Note that both works of adhesion W_{SL} and W_{SV} are positive, and we will discuss about them later from a viewpoint of the free energy as well as the curvature effects. With the decrease in the radius R_{s}, both $-(\gamma_{\mathrm{SL}} - \gamma_{\mathrm{S0}})$ and $-(\gamma_{\mathrm{SV}} - \gamma_{\mathrm{S0}})$ became smaller, and the dependence was more remarkable for the larger η value. For the smallest cylinder with $R_{\mathrm{s}} = 0.777$ nm, $-(\gamma_{\mathrm{SL}} - \gamma_{\mathrm{S0}})$ was about 2×10^{-3} N/m smaller than that of the flat plate. However, $-(\gamma_{\mathrm{SV}} - \gamma_{\mathrm{S0}})$ was also reduced with the decrease of R_{s}, and this resulted in the rather small dependence of the contact angle on the radius shown in Fig. 3.

C. Applicability of Young's equation

Using the relative interfacial tensions $\gamma_{\mathrm{SL}} - \gamma_{\mathrm{S0}}$ and $\gamma_{\mathrm{SV}} - \gamma_{\mathrm{S0}}$ obtained in Subsection III B, we examined whether Young's equation holds for the present system with a curved solid surface. Figure 7 shows the comparison between the apparent contact angle cosine $\cos\theta_{\mathrm{app}}$ in Fig. 3 determined from the meniscus shape and that estimated by Young's equation (1) defined by

$$\cos\theta_{\mathrm{Y}} = \frac{\gamma_{\mathrm{SV}} - \gamma_{\mathrm{SL}}}{\gamma_{\mathrm{LV}}} \equiv \frac{(\gamma_{\mathrm{SV}} - \gamma_{\mathrm{S0}}) - (\gamma_{\mathrm{SL}} - \gamma_{\mathrm{S0}})}{\gamma_{\mathrm{LV}}} = \frac{W_{\mathrm{SL}} - W_{\mathrm{SV}}}{\gamma_{\mathrm{LV}}} - 1, \tag{24}$$

using the interfacial tensions obtained above via the mechanical route. Note that γ_{LV} was set constant, considering that its curvature dependence appeared only for a radius of curvature smaller than about $3\sigma_{\mathrm{ff}}$ for the LJ fluid,[58] which is smaller than that in the present study. In addition, it has been shown that γ_{LV} consistent

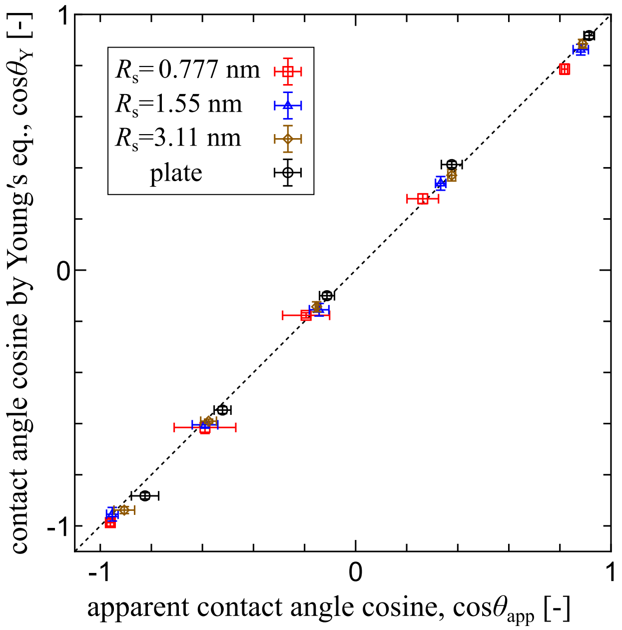

FIG. 7. Comparison between the apparent contact angle $\cos\theta_\mathrm{app}$ and that estimated by Young's equation $\cos\theta_\mathrm{Y}$ using the interfacial tensions obtained by the mechanical route. The value of η ranges from 0.03 to 0.15 for each cylinder radius R_s and plate.

with Young's equation should be defined at a position excluding the adsorption layers around the SL interface[28] at which the radius of curvature of the LV interface is sufficiently large and the curvature effect is negligible. For the whole range of η values and radii R_s tested, $\cos\theta_\mathrm{app}$ and $\cos\theta_\mathrm{Y}$ agreed very well, and this indicates that Young's equation holds for the present systems with curved solid surfaces without pinning if the solid-related relative interfacial tensions $\gamma_\mathrm{SL}-\gamma_\mathrm{S0}$ and $\gamma_\mathrm{SV}-\gamma_\mathrm{S0}$ are properly evaluated via a mechanical route.

D. Discussion

A question arises: why was the curvature dependence of the relative interfacial tensions $\gamma_\mathrm{SL}-\gamma_\mathrm{S0}$ and $\gamma_\mathrm{SV}-\gamma_\mathrm{S0}$ shown in Fig. 6 not so large compared to the contact-line force $\xi_z^\mathrm{cl}=-u_\mathrm{SL}+u_\mathrm{SV}$ seen in Fig. 5? More specifically, why did $-u_\mathrm{SL}$ in the left panel of Fig. 5 and $-(\gamma_\mathrm{SL}-\gamma_\mathrm{S0})$ in Fig. 6 show opposite dependence on R_s? To examine the curvature dependence of $-u_\mathrm{SL}$, we evaluated the density field around the solid–liquid interface, where we have carried out an additional simulation with a solid cylinder with a chiral index (60,0) (R_s = 2.33 nm). Figure 8 shows the comparison of the fluid density around a solid–liquid interface between the (a) cylinder with R_s = 0.777 nm and (b) flat plate with η = 0.15. Positions of the solid particles are shown with small black and gray circles, where the particles with the same color are at the same height z, and the distance range of r_sf from a black solid particle satisfying interaction potential $\Phi_\mathrm{sf}(r_\mathrm{sf})\le-\epsilon_\mathrm{sf}/2$, as indicated by the blue potential graph, is depicted by magenta circles. As shown in this figure, the high density region in red corresponding to the fluid first adsorption layer is included in this distance range more for R_s = 0.777 nm, and this results in the higher $-u_\mathrm{SL}$ for smaller R_s indicated in the left panel of Fig. 5 because the fluid particles in this distance range have the main contribution.[53,67] On the other hand, smaller $-u_\mathrm{SV}$ for smaller R_s was due to the lower density on a solid with a smaller radius. This is because for the fluid particles adsorbed onto the solid, the mean potential field formed by the solid particles has a shallower well on a solid with a smaller radius than on a flat surface, and the fluid particles can easily be desorbed.

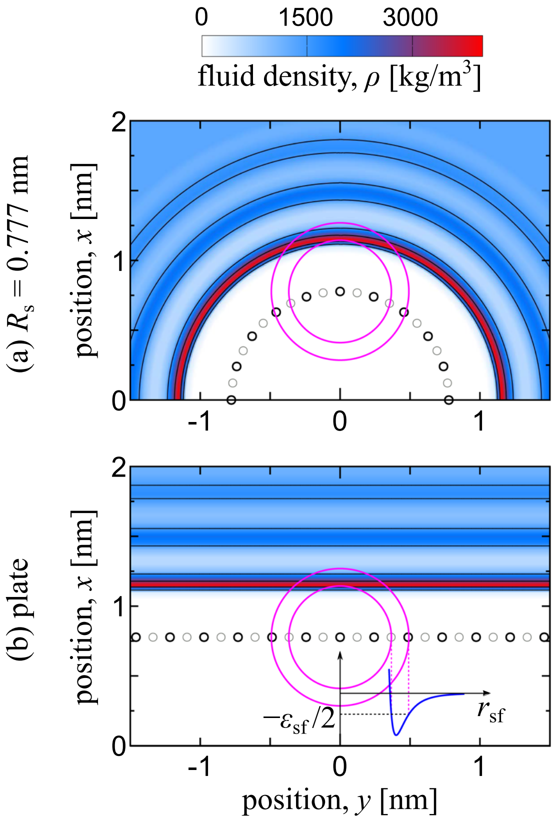

FIG. 8. Comparison of the fluid density around a solid–liquid interface between the (a) cylinder with R_s = 0.777 nm and (b) flat plate with η = 0.15. Positions of the solid particles are shown with small black and gray circles, and the distance range of r_sf from a solid particle satisfying the interaction potential $\Phi_\mathrm{sf}(r_\mathrm{sf})\le-\epsilon_\mathrm{sf}/2$ is depicted by magenta circles.

Different from the average SL interaction potential $-u_\mathrm{SL}$, the relative interfacial tension is considered the interfacial free energy per area, i.e., $\gamma_\mathrm{SL}-\gamma_\mathrm{S0}$ is related to the SL work of adhesion W_SL in Eq. (22), and it consists of internal energy and entropy terms,[35,36]

$$W_\mathrm{SL}=-(\gamma_\mathrm{SL}-\gamma_\mathrm{S0})+\gamma_\mathrm{LV}=-u_\mathrm{SL}-(-T\Delta s_\mathrm{SL}), \qquad (25)$$

where $-T\Delta s_\mathrm{SL}$ is due to the entropy "loss" $-\Delta s_\mathrm{SL}$ induced by the density increase in the adsorption layers of the SL interface. Figure 9 shows the solid–liquid interfacial potential energy per area $-u_\mathrm{SL}$, the work of adhesion W_SL, and the entropy loss $-T\Delta s_\mathrm{SL}$ in Eq. (25) for various cylinder radii R_s with η = 0.15. Note that the additional data

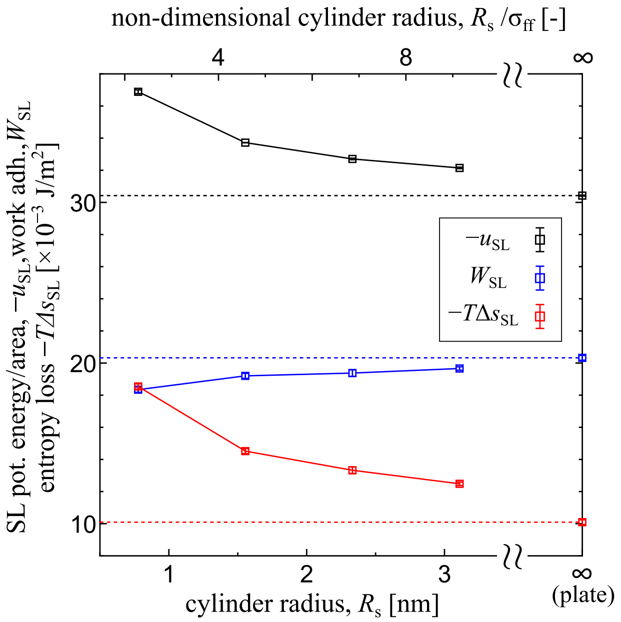

FIG. 9. Solid–liquid interfacial potential energy per area $-u_{SL}$, the work of adhesion W_{SL}, and the entropy loss $-T\Delta s_{SL}$ calculated by Eq. (25) for various cylinder radii R_s with a solid–fluid interaction parameter $\eta = 0.15$.

for a cylinder radius $R_s = 2.33$ nm were also shown, and the radius for the plate was set as $R_s = \infty$. A larger entropy loss exceeding the potential gain in $-u_{SL}$ resulted in the opposite curvature dependence between the SL interfacial potential energy $-u_{SL}$ and the relative interfacial tension $-(\gamma_{SL} - \gamma_{S0})$ shown in Figs. 5 and 6. In addition, it is indicated that the curvature effect could remain even for a relatively large cylinder radius R_s larger than about $10\sigma_{ff}$, which is much larger than the radius dependence range of γ_{LV} reported for the LJ droplets.[58]

IV. CONCLUDING REMARKS

In this study, we successfully extracted the SL and SV interfacial tensions of a simple Lennard-Jones fluid around a solid cylinder with a nanometer-scale diameter by extending the theoretical nano-Wilhelmy equations for a quasi-two-dimensional flat solid plate from our previous study.[26] The solid-liquid (SL) and solid-vapor (SV) interfacial tensions were calculated from the integral of the normal-stress in the wall-tangential direction by considering the mechanical force balances on control volumes set around the bottom and top ends of the solid cylinder subject to the fluid stress and external force from the solid, where the local force on the solid around the contact line expressed by these external forces agreed well with the analytical expression. The theoretical contact angle calculated by Young's equation using these interfacial tensions agreed well with the apparent contact angle estimated by the analytical solution to fit the meniscus shape, showing that Young's equation holds even for menisci around solids with nanoscale curvature if the interfacial tensions are properly evaluated. It was also shown that the curvature dependence of the SL and SV interfacial tensions as the free energy was different from that of the corresponding interaction potential energies as a part of the internal energy, which explains the weak curvature dependence of the contact angle in the present results.

The accurate calculation of the interfacial tensions on curved surfaces could explain the unique wetting behavior of water on carbon nanotubes (CNTs), e.g., the temperature dependence of the SV interface structure[52] and the diameter dependence of the capillary force[53] outside the CNTs as well as the phase change of water in the CNTs[70] indicated in experiments. In addition, it should enable the exploration of the Tolman equation for the solid-related interfaces. Related to this, an interesting future target is the interfacial tensions inside the curved interface from a mechanical route, which should enable the analysis of nano-confinement effects or nanoscale capillaries as well, e.g., in carbon nanotubes.

ACKNOWLEDGMENTS

H.K., T.O., and Y.Y. were supported by the JSPS KAKENHI (Grant Nos. JP20J20251, JP18K03929, and JP18K03978, respectively), Japan. Y.Y. was also supported by the JST CREST (Grant No. JPMJCR18I1), Japan.

AUTHOR DECLARATIONS

Conflict of Interest

The authors have no conflicts to disclose.

DATA AVAILABILITY

The data that support the findings of this study are available from the corresponding author upon reasonable request.

APPENDIX A: EXTENDED BAKKER's EQUATION FOR CYLINDER

We formulate the relative solid–liquid (SL) interfacial tension relative to the solid–vacuum (S0) $\gamma_{SL} - \gamma_{S0}$ between cylindrical solid surface and liquid through the thought experiment shown in Fig. 10. The side piston normal to the cylinder axis z is in contact only with the liquid, i.e., the inner radius is at r_{SL} set at the limit radius nearest to the solid that the fluid particle can reach, whereas the outer radius $r_{\mathrm{L}}^{\mathrm{blk}}$ is at the liquid bulk sufficiently away from the SL interface. The axis-normal stress defined by

$$\tau_{zz}(r) \equiv -p_z(r) \tag{A1}$$

is a function of the radial position r, and it satisfies

$$p_z(r) = p_{\mathrm{L}}^{\mathrm{blk}} = \text{const.} \quad (r \ge r_{\mathrm{L}}^{\mathrm{blk}}). \tag{A2}$$

On the other hand, the top piston is set at the liquid bulk on which homogeneous pressure identical to the bulk pressure $p_{\mathrm{L}}^{\mathrm{blk}}$ is exerted. We suppose a virtual infinitesimal displacement δz of the side piston with a simultaneous downward displacement of the top piston so that the liquid volume may not change. If the operation is quasi-static at a constant temperature, the change in the Helmholtz free energy δF is equal to the work δW exerted on the system given by

$$\delta F = \delta W = p_{\mathrm{L}}^{\mathrm{blk}}\delta V - 2\pi\delta z \int_{r_{SL}}^{r_{\mathrm{L}}^{\mathrm{blk}}} \mathrm{d}r\, p_z(r) r, \tag{A3}$$

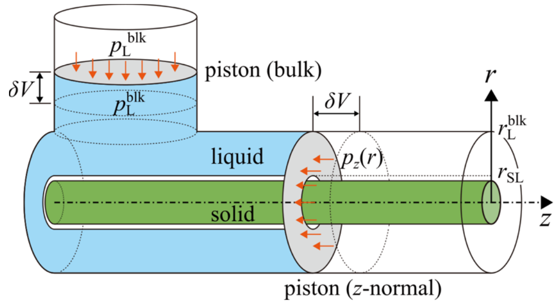

FIG. 10. Thought experiment for the connection between relative solid–liquid interfacial tension and pressure distribution around the solid cylinder.

where the volume increase and decrease δV due to the motions of side and top pistons, respectively, writes

$$\delta V = 2\pi\delta z\int_{r_{\rm SL}}^{r_{\rm L}^{\rm blk}} {\rm d}r\, r = \pi\Big[\big(r_{\rm L}^{\rm blk}\big)^2 - r_{\rm SL}^2\Big]\delta z. \tag{A4}$$

The free energy change δF in Eq. (A3) is uniquely defined as long as $r_{\rm L}^{\rm blk}$ is set in the bulk satisfying Eq. (A2). From a macroscopic point of view, the SL interface is increased and the S0 interface is reduced with this operation. By assuming that the SL interface is at $r_{\rm SL}$, it follows that

$$\delta F = 2\pi r_{\rm SL}(\gamma_{\rm SL} - \gamma_{\rm S0})\delta z. \tag{A5}$$

By equating Eqs. (A3) and (A5), the following relation is derived as extended Bakker's equation for a cylindrical SL interface:

$$\gamma_{\rm SL} - \gamma_{\rm S0} = \frac{1}{r_{\rm SL}}\left[\int_{r_{\rm SL}}^{r_{\rm L}^{\rm blk}} {\rm d}r\,\tau_{zz}(r)r + \frac{p_{\rm L}^{\rm blk}\big[\big(r_{\rm L}^{\rm blk}\big)^2 - r_{\rm SL}^2\big]}{2}\right], \tag{A6}$$

where Eq. (A1) is used as well. Equation (A6) means that the relative SL interfacial tension is obtained with the stress integral, bulk pressure, and the interface position.

The relative solid–vapor (SV) interfacial tension is expressed as well by

$$\gamma_{\rm SV} - \gamma_{\rm S0} = \frac{1}{r_{\rm SV}}\left[\int_{r_{\rm SV}}^{r_{\rm V}^{\rm blk}} {\rm d}r\,\tau_{zz}(r)r + \frac{p_{\rm V}^{\rm blk}\big[\big(r_{\rm V}^{\rm blk}\big)^2 - r_{\rm SV}^2\big]}{2}\right]. \tag{A7}$$

APPENDIX B: EXTRACTION OF THE INTERACTION FORCE BETWEEN THE LIQUID AND SOLID ACROSS A *z*-NORMAL PLANE AT A SL INTERFACE

We derive the interaction force $F_z^{\rm diag(SL)}$ exemplified in the bottom panels of Fig. 4, namely, the interaction force between the solid above a z-normal plane $z = z_{\rm SL}$ and liquid below that plane. The plane $z = z_{\rm SL}$ is at a height around which the fluid density is independent of the position z because the plane is sufficiently away from the contact line and the bottom of the cylinder.

Taking into account that the solid is supposed to be smooth for the fluid particles because the inter-particle distance parameters $\sigma_{\rm ff}$ and $\sigma_{\rm sf}$ are sufficiently large compared to $r_{\rm ss}$ between solid particles, the solid–liquid interaction force can be analytically modeled by assuming the mean fields of the fluid and solid. The mean number density per volume $\rho_V^{\rm f}(r_{\rm f})$ $(= \rho/m_{\rm f})$ of the fluid is given as a function of the radial position $r_{\rm f}$ of the fluid, whereas a constant mean number density per area $\rho_A^{\rm s}$ of the solid at $r = R_{\rm s}$ is used considering the present system with a solid cylinder of zero-thickness without volume; however, the following derivation can easily be extended for a system with a solid with a volume and density per volume in the range $r \le R_{\rm s}$.

We start from the potential energy on a solid particle at position $(R_{\rm s}, \vartheta_{\rm s}, z_{\rm s})$ due to a fluid particle at $(r_{\rm f}, \vartheta_{\rm f}, z_{\rm f})$, both in the cylindrical $r\vartheta z$-coordinate, given by Eq. (2). Assuming that the fluid particles are homogeneously distributed in the azimuth direction ϑ with a number density $\rho_V^{\rm f}(r_{\rm f}, z_{\rm f})$ per volume, the mean potential field from an infinitesimal fluid volume segment of ${\rm d}z_{\rm f} \times 2\pi r_{\rm f}{\rm d}r_{\rm f}$ on a solid particle is defined by using $\rho_V^{\rm f}(z_{\rm f}, r_{\rm f})$ and the mean local potential $\phi(z'_{\rm f}, r'_{\rm f})$ as $\rho_V^{\rm f}(z_{\rm f}, x_{\rm f}){\rm d}z_{\rm f}{\rm d}r_{\rm f}\cdot\phi(z'_{\rm f}, r'_{\rm f})$, where $\phi(z'_{\rm f}, r'_{\rm f})$ is given by

$$\phi(z'_{\rm f}, r'_{\rm f}) \equiv \int_0^{2\pi} \Phi^{\rm LJ}(r_{\rm sf})r_{\rm f}{\rm d}\vartheta_{\rm f}, \tag{B1}$$

where we define

$$r_{\rm sf} = \sqrt{(r_{\rm f}\cos\vartheta_{\rm f} - R_{\rm s}\cos\vartheta_{\rm s})^2 + (r_{\rm f}\sin\vartheta_{\rm f} - R_{\rm s}\sin\vartheta_{\rm s})^2 + z'^2_{\rm f}}, \tag{B2}$$

and

$$z'_{\rm f} \equiv z_{\rm f} - z_{\rm s} \equiv -z'_{\rm s}, \qquad r'_{\rm f} \equiv r_{\rm f} - R_{\rm s}. \tag{B3}$$

Then, the local force in the z-direction $f_z^{\rm s}(z'_{\rm f}, r'_{\rm f}){\rm d}z_{\rm f}{\rm d}r_{\rm f}{\rm d}z_{\rm s}$ exerted on the solid cylinder in $[z_{\rm s}, z_{\rm s} + {\rm d}z_{\rm s}]$ with an area number density of the solid particles $\rho_A^{\rm s}(z_{\rm s})$ from the present fluid volume segment is given by

$$\begin{aligned} f_z^{\rm s}(z_{\rm s}, z_{\rm f}, r_{\rm f}){\rm d}z_{\rm f}{\rm d}r_{\rm f}{\rm d}z_{\rm s} = {}& -\rho_V^{\rm f}(z_{\rm f}, r_{\rm f})\frac{\partial\phi(z'_{\rm f}, r'_{\rm f})}{\partial z_{\rm s}} \\ & \times {\rm d}z_{\rm f}{\rm d}r_{\rm f}\cdot 2\pi R_{\rm s}\rho_A^{\rm s}(z_{\rm s}){\rm d}z_{\rm s}, \end{aligned} \tag{B4}$$

where

$$f_z^{\rm s}(z_{\rm s}, z_{\rm f}, r_{\rm f}) = -2\pi R_{\rm s}\rho_A^{\rm s}(z_{\rm s})\rho_V^{\rm f}(z_{\rm f}, r_{\rm f})\frac{\partial\phi(z'_{\rm f}, r'_{\rm f})}{\partial z_{\rm s}} \tag{B5}$$

denotes the axial force density on the solid given as a function of $z_{\rm s}$, $z_{\rm f}$, and $r_{\rm f}$.

Since $\Phi_{\rm LJ}(r_{\rm sf})$ is truncated at the cutoff distance $r_{\rm c}$ in the present case,

$$\phi\left(z'_{\mathrm{f}}, r'_{\mathrm{f}}\right) = 0, \quad \frac{\partial \phi\left(z'_{\mathrm{f}}, r'_{\mathrm{f}}\right)}{\partial z_{\mathrm{s}}} = 0$$

for

$$|z'_{\mathrm{f}}| \geq \sqrt{r_{\mathrm{c}}^2 - r'^2_{\mathrm{f}}} \equiv z_{\mathrm{c}}\left(r'_{\mathrm{f}}\right) \quad \text{or} \quad r'_{\mathrm{f}} \geq r_{\mathrm{c}} \tag{B6}$$

holds, where $z_{\mathrm{c}}\left(r'_{\mathrm{f}}\right)$ as a function of r'_{f} denotes the cutoff with respect to z'_{f}. This cutoff is not critical as long as $\phi\left(z'_{\mathrm{f}}, r'_{\mathrm{f}}\right)$ quickly vanishes with the increase of r, but we continue the derivation including the cutoff for simplicity. With the definition of r_{SF} as the limit that the fluid could reach, it follows that

$$\rho_V^{\mathrm{f}} = 0 \quad \text{for} \quad r_{\mathrm{f}} < r_{\mathrm{SF}}. \tag{B7}$$

In addition, considering that $\phi(z'_{\mathrm{f}}, r'_{\mathrm{f}})$ is an even function with respect to z'_{f}, i.e.,

$$\phi\left(z'_{\mathrm{f}}, r'_{\mathrm{f}}\right) = \phi(-z'_{\mathrm{f}}, r'_{\mathrm{f}}), \tag{B8}$$

it follows for the mean local potential ϕ that

$$\frac{\partial \phi\left(z'_{\mathrm{f}}, r'_{\mathrm{f}}\right)}{\partial z_{\mathrm{s}}} = -\frac{\partial \phi\left(-z'_{\mathrm{f}}, r'_{\mathrm{f}}\right)}{\partial z_{\mathrm{s}}} \tag{B9}$$

and

$$\frac{\partial \phi\left(z'_{\mathrm{f}}, r'_{\mathrm{f}}\right)}{\partial z_{\mathrm{s}}} = -\frac{\partial \phi\left(z'_{\mathrm{f}}, r'_{\mathrm{f}}\right)}{\partial z_{\mathrm{f}}}, \tag{B10}$$

where Eq. (B3) is applied for the latter. This corresponds to the action–reaction relation between solid and fluid particles under a simple two-body interaction, i.e.,

$$\begin{aligned} f_z^{\mathrm{f}}(z_{\mathrm{s}}, z_{\mathrm{f}}, r_{\mathrm{f}}) &= -f_z^{\mathrm{s}}(z_{\mathrm{s}}, z_{\mathrm{f}}, r_{\mathrm{f}}) \\ &= -2\pi R_{\mathrm{s}} \rho_A^{\mathrm{s}}(z_{\mathrm{s}}) \rho_V^{\mathrm{f}}(z_{\mathrm{f}}, r_{\mathrm{f}}) \frac{\partial \phi\left(z'_{\mathrm{f}}, r'_{\mathrm{f}}\right)}{\partial z_{\mathrm{f}}} \end{aligned} \tag{B11}$$

holds for the tangential force density on the fluid f_z^{f}.

Based on these properties, we now derive the analytical expression of the force exerted on the solid above a z-normal plane $z = z_{\mathrm{SL}}$ from the liquid below that plane, i.e., the force of interest $F_z^{\mathrm{diag(SL)}}$ given by

$$\begin{aligned} F_z^{\mathrm{diag(SL)}} &= \int_0^{r_{\mathrm{c}}} \mathrm{d}r'_{\mathrm{f}} \int_{-z_{\mathrm{c}}(r'_{\mathrm{f}})}^{0} \mathrm{d}z'_{\mathrm{f}} \int_{-z'_{\mathrm{f}}}^{z_{\mathrm{c}}(r'_{\mathrm{f}})} \mathrm{d}z'_{\mathrm{s}} f_z^{\mathrm{f}} \\ &= -\int_0^{r_{\mathrm{c}}} \mathrm{d}r'_{\mathrm{f}} \left[\int_{-z_{\mathrm{c}}(r'_{\mathrm{f}})}^{0} \mathrm{d}z'_{\mathrm{f}} \left(\int_{-z'_{\mathrm{f}}}^{z_{\mathrm{c}}(r'_{\mathrm{f}})} \mathrm{d}z'_{\mathrm{s}} f_z^{\mathrm{s}} \right) \right], \end{aligned} \tag{B12}$$

where the double integral in the square brackets corresponds to the top-left region in Fig. 11. Let the density ρ_V^{f} for $z_{\mathrm{SL}} - z_{\mathrm{c}} < z_{\mathrm{f}} < z_{\mathrm{SL}} + z_{\mathrm{c}}$ be given as a unique function of r_{f} by

$$\rho_V^{\mathrm{f}}(z_{\mathrm{f}}, r_{\mathrm{f}}) = \rho_V^{\mathrm{f(SL)}}(r_{\mathrm{f}}). \tag{B13}$$

Then, it follows for the double integral in the square brackets in Eq. (B12) that

$$\begin{aligned} \int_{-z_{\mathrm{c}}}^{0} \mathrm{d}z'_{\mathrm{f}} \left(\int_{-z'_{\mathrm{f}}}^{z_{\mathrm{c}}} \mathrm{d}z'_{\mathrm{s}} f_z^{\mathrm{s}} \right) &= -2\pi R_{\mathrm{s}} \int_{-z_{\mathrm{c}}}^{0} \mathrm{d}z'_{\mathrm{f}} \rho_V^{\mathrm{f(SL)}}(r'_{\mathrm{f}}) \left[\int_{-z'_{\mathrm{f}}}^{z_{\mathrm{c}}} \mathrm{d}z'_{\mathrm{s}} \rho_A^{\mathrm{s}}(z_{\mathrm{s}}) \frac{\partial \phi(z'_{\mathrm{f}}, r'_{\mathrm{f}})}{\partial z_{\mathrm{s}}} \right] \\ &= -2\pi R_{\mathrm{s}} \int_{-z_{\mathrm{c}}}^{0} \rho_V^{\mathrm{f(SL)}}(r'_{\mathrm{f}}) \mathrm{d}z'_{\mathrm{f}} \left\{ \left[\rho_A^{\mathrm{s}}(z_{\mathrm{s}}) \phi(z'_{\mathrm{f}}, r'_{\mathrm{f}}) \right]_{z'_{\mathrm{s}}=-z'_{\mathrm{f}}}^{z_{\mathrm{c}}} - \int_{-z'_{\mathrm{f}}}^{z_{\mathrm{c}}} \mathrm{d}z'_{\mathrm{s}} \frac{d\rho_A^{\mathrm{s}}(z_{\mathrm{s}})}{dz_{\mathrm{s}}} \phi(z'_{\mathrm{f}}, r'_{\mathrm{f}}) \right\} \\ &= 2\pi R_{\mathrm{s}} \int_{-z_{\mathrm{c}}}^{0} \mathrm{d}z'_{\mathrm{f}} \rho_V^{\mathrm{f(SL)}}(r'_{\mathrm{f}}) \left[\rho_A^{\mathrm{s}}(-z'_{\mathrm{f}}) \phi(-z'_{\mathrm{f}}, r'_{\mathrm{f}}) + \int_{-z'_{\mathrm{f}}}^{z_{\mathrm{c}}} \mathrm{d}z'_{\mathrm{s}} \frac{d\rho_A^{\mathrm{s}}(z_{\mathrm{s}})}{dz_{\mathrm{s}}} \phi(z'_{\mathrm{f}}, r'_{\mathrm{f}}) \right], \\ &= 2\pi R_{\mathrm{s}} \int_{-z_{\mathrm{c}}}^{0} \mathrm{d}z'_{\mathrm{f}} \rho_V^{\mathrm{f(SL)}}(r'_{\mathrm{f}}) \rho_A^{\mathrm{s}}(-z'_{\mathrm{f}}) \phi(z'_{\mathrm{f}}, r'_{\mathrm{f}}) \\ &\quad + 2\pi R_{\mathrm{s}} \int_{-z_{\mathrm{c}}}^{0} \mathrm{d}z'_{\mathrm{f}} \rho_V^{\mathrm{f(SL)}}(r'_{\mathrm{f}}) \left[\int_{-z'_{\mathrm{f}}}^{z_{\mathrm{c}}} \mathrm{d}z'_{\mathrm{s}} \frac{d\rho_A^{\mathrm{s}}(z_{\mathrm{s}})}{dz_{\mathrm{s}}} \phi(z'_{\mathrm{f}}, r'_{\mathrm{f}}) \right], \end{aligned} \tag{B14}$$

where $\phi(z_{\mathrm{c}}, r'_{\mathrm{f}}) = 0$ and Eq. (B8) are used for the fourth equality. With an additional assumption of

$$\rho_A^{\mathrm{s}} = \text{const.}, \tag{B15}$$

the second term of the right-hand side becomes zero, and it follows

$$\begin{aligned} \int_{-z_{\mathrm{c}}}^{0} \mathrm{d}z'_{\mathrm{f}} \left(\int_{-z'_{\mathrm{f}}}^{z_{\mathrm{c}}} \mathrm{d}z'_{\mathrm{s}} f_z^{\mathrm{s}} \right) &= 2\pi R_{\mathrm{s}} \rho_A^{\mathrm{s}} \int_{-z_{\mathrm{c}}}^{0} \mathrm{d}z'_{\mathrm{f}} \rho_V^{\mathrm{f(SL)}}(r'_{\mathrm{f}}) \phi(z'_{\mathrm{f}}, r'_{\mathrm{f}}) \\ &= \pi R_{\mathrm{s}} \rho_A^{\mathrm{s}} \int_{-z_{\mathrm{c}}}^{z_{\mathrm{c}}} \mathrm{d}z'_{\mathrm{f}} \rho_V^{\mathrm{f(SL)}}(r'_{\mathrm{f}}) \phi(z'_{\mathrm{f}}, r'_{\mathrm{f}}), \end{aligned} \tag{B16}$$

considering that ϕ is an even function with respect to z'_{f} for the second equality. By inserting Eq. (B16) into Eq. (B12), it follows

$$F_z^{\mathrm{diag(SL)}} = -\pi R_{\mathrm{s}} \rho_A^{\mathrm{s}} \int_0^{r_{\mathrm{c}}} \mathrm{d}r'_{\mathrm{f}} \int_{-z_{\mathrm{c}}(r'_{\mathrm{f}})}^{z_{\mathrm{c}}(r'_{\mathrm{f}})} \mathrm{d}z'_{\mathrm{f}} \rho_V^{\mathrm{f(SL)}}(r'_{\mathrm{f}}) \phi(z'_{\mathrm{f}}, r'_{\mathrm{f}}). \tag{B17}$$

Indeed, the RHS of Eq. (B17) can be expressed using the following SL potential energy density u_{SL} given by

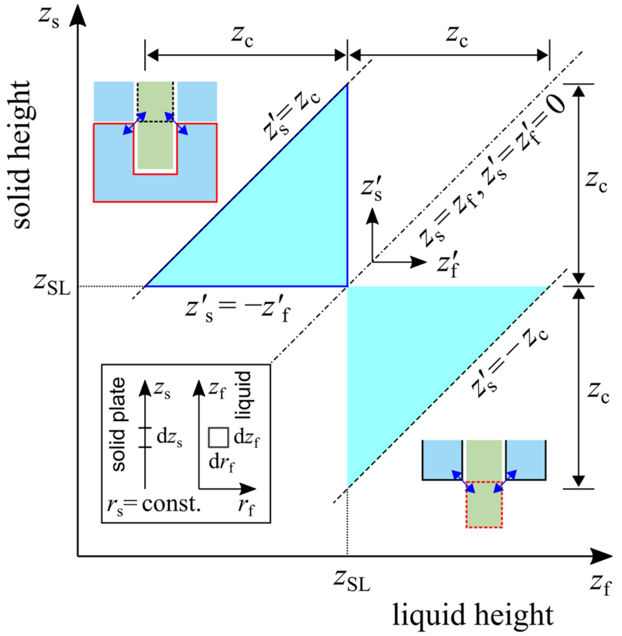

FIG. 11. Region for the double integral of the mean field to calculate the interaction between the solid cylinder above $z_s = z^{SL}$ and liquid below $z_f = z^{SL}$ (top-left triangle in the solid blue line). The geometrical relation is shown in the inset. The cutoff distance z_c for $|z_f - z_s|$ depends on the relative radial position $r_f - R_s$.

$$u_{SL} \equiv \rho_A^s \int_0^{r_c} dr'_f \int_{-z_c(r'_f)}^{z_c(r'_f)} dz'_f \rho_V^{f(SL)}(r'_f)\phi(z'_f, r'_f), \tag{B18}$$

which represents the SL potential energy per solid area at the SL interface away both from the CL and from the bottom of the solid plate. With u_{SL}, Eq. (B17) writes

$$F_z^{\text{diag(SL)}} = -\pi R_s u_{SL}, \tag{B19}$$

which corresponds to Eq. (13) in the main text.

Similar to $F_z^{\text{diag(SL)}}$, the interaction force $F_z^{\text{diag(SV)}}$ between the solid above a z-normal plane $z = z_{SV}$ and the vapor below that plane writes

$$F_z^{\text{diag(SV)}} = -\pi R_s u_{SV}, \tag{B20}$$

where the SV potential energy density u_{SV} is given by

$$u_{SV} \equiv \rho_A^s \int_0^{r_c} dr'_f \rho_V^{f(SV)}(r'_f) \int_{-z_c(r'_f)}^{z_c(r'_f)} dz'_f \phi(z'_f, r'_f). \tag{B21}$$

APPENDIX C: EXTRACTION OF THE FORCE EXERTED ON THE SOLID AROUND THE CONTACT LINE

We can formulate the downward force on the solid around the contact line $2\pi R_s \xi_z^{cl}$ from the fluid as the reaction force, i.e., the upward force on the liquid from the solid, from the force balance similar to that displayed in Fig. 4. Let F_z^{cl} be the force on the liquid around the contact line, $2\pi R_s \xi_z^{cl}$ can be obtained by adding $F_z^{\text{diag(SL)}} - F_z^{\text{diag(SV)}}$ and subtracting $-F_z^{\text{diag(SL)}} + F_z^{\text{diag(SV)}}$ as

$$2\pi R_s \xi_z^{cl} = F_z^{cl} + 2\left(F_z^{\text{diag(SL)}} - F_z^{\text{diag(SV)}}\right), \tag{C1}$$

as illustrated in Fig. 12. In case the solid surface is smooth and flat and no pinning is induced,

$$F_z^{cl} = 0 \tag{C2}$$

holds because the average surface lateral force on each fluid particles from the solid is zero.[26,28,29,36] This condition is applicable to the present systems. By inserting Eqs. (13), (14), and (C2) into Eq. (C1),

$$\xi_z^{cl} = -u_{SL} + u_{SV} = (-u_{SL}) - (-u_{SV}) \tag{C3}$$

is derived as the analytical expression of ξ_z^{cl} in Eq. (15) in the main text, where the final expression is to emphasize that the potential energy densities u_{SL} and u_{SV} are both negative.

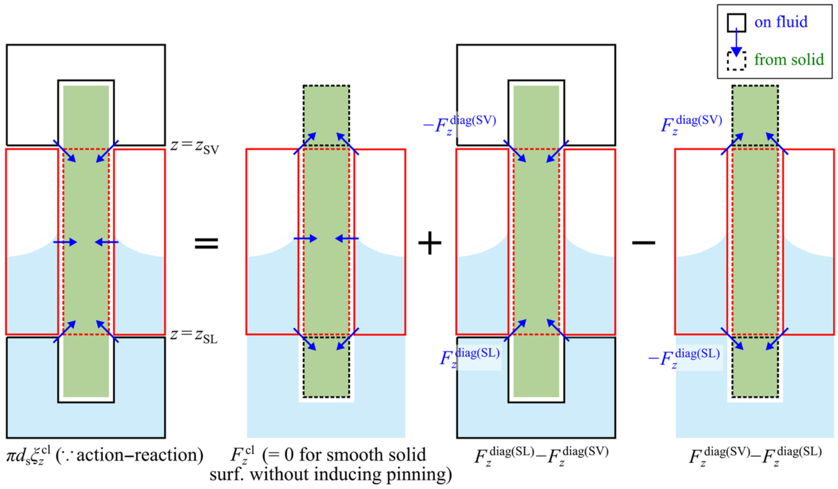

FIG. 12. Schematic of the extraction of the z-direction force on the solid around the contact line from the fluid.

REFERENCES

[1] P. G. de Gennes, “‘Wetting’ statics and dynamics,” Rev. Mod. Phys. **57**, 827–863 (1985).

[2] S. Ono and S. Kondo, *Molecular Theory of Surface Tension in Liquids*, Encyclopedia of Physics/Handbuch der Physik (Springer, 1960), pp. 134–280.

[3] J. S. Rowlinson and B. Widom, *Molecular Theory of Capillarity* (Dover, 1982).

[4] L. Schimmele, M. Napiórkowski, and S. Dietrich, “Conceptual aspects of line tensions,” J. Chem. Phys. **127**, 164715 (2007).

[5] J. W. Drelich, L. Boinovich, E. Chibowski, C. D. Volpe, L. Hołysz, A. Marmur, and S. Siboni, “Contact angles: History of over 200 years of open questions,” Surf. Innovations **8**, 3 (2019).

[6] T. Young, “An essay on the cohesion of fluids,” Philos. Trans. R. Soc. London **95**, 65 (1805).

[7] L. Gao and T. J. McCarthy, “Wetting 101°,” Langmuir **25**, 14105–14115 (2009).

[8] M. N. Popescu, G. Oshanin, S. Dietrich, and A.-M. Cazabat, “Precursor films in wetting phenomena,” J. Phys.: Condens. Matter **24**, 243102 (2012).

[9] L. R. White, “On deviations from Young's equation,” J. Chem. Soc., Faraday Trans. 1 **73**, 390–398 (1977).

[10] L. Boruvka and A. W. Neumann, “Generalization of the classical theory of capillarity,” J. Chem. Phys. **66**, 5464–5476 (1977).

[11] A. Marmur, “Line tension and the intrinsic contact angle in solid–liquid–fluid systems,” J. Colloid Interface Sci. **186**, 462–466 (1997).

[12] V. K. Kumikov and K. B. Khokonov, “On the measurement of surface free energy and surface tension of solid metals,” J. Appl. Phys. **54**, 1346–1350 (1983).

[13] W. R. Tyson and W. A. Miller, “Surface free energies of solid metals: Estimation from liquid surface tension measurements,” Surf. Sci. **62**, 267–276 (1977).

[14] J. G. Kirkwood and F. P. Buff, “The statistical mechanical theory of surface tension,” J. Chem. Phys. **17**, 338–343 (1949).

[15] G. Bakker, *Kapillarität und Oberflächenspannung* (Wien-Harms, 1928), Vol. 6.

[16] M. P. Allen and D. J. Tildesley, *Computer Simulation of Liquids* (Oxford University Press, 1987).

[17] J. Z. Tang and J. G. Harris, “Fluid wetting on molecularly rough surfaces,” J. Chem. Phys. **103**, 8201–8208 (1995).

[18] G. J. Gloor, G. Jackson, F. J. Blas, and E. De Miguel, “Test-area simulation method for the direct determination of the interfacial tension of systems with continuous or discontinuous potentials,” J. Chem. Phys. **123**, 134703 (2005).

[19] T. Ingebrigtsen and S. Toxvaerd, “Contact angles of Lennard-Jones liquids and droplets on planar surfaces,” J. Phys. Chem. C **111**, 8518–8523 (2007).

[20] S. K. Das and K. Binder, “Does Young's equation hold on the nanoscale? A Monte Carlo test for the binary Lennard-Jones fluid,” Europhys. Lett. **92**, 26006 (2010).

[21] J. H. Weijs, A. Marchand, B. Andreotti, D. Lohse, and J. H. Snoeijer, “Origin of line tension for a Lennard-Jones nanodroplet,” Phys. Fluids **23**, 022001 (2011).

[22] D. Seveno, T. D. Blake, and J. de Coninck, “Young's equation at the nanoscale,” Phys. Rev. Lett. **111**, 096101 (2013).

[23] M. J. P. Nijmeijer and J. M. J. van Leeuwen, “Microscopic expressions for the surface and line tension,” J. Phys. A: Math. Gen. **23**, 4211–4235 (1990).

[24] M. J. P. Nijmeijer, C. Bruin, A. F. Bakker, and J. M. J. van Leeuwen, “Wetting and drying of an inert wall by a fluid in a molecular-dynamics simulation,” Phys. Rev. A **42**, 6052–6059 (1990).

[25] S. Nishida, D. Surblys, Y. Yamaguchi, K. Kuroda, M. Kagawa, T. Nakajima, and H. Fujimura, “Molecular dynamics analysis of multiphase interfaces based on *in situ* extraction of the pressure distribution of a liquid droplet on a solid surface,” J. Chem. Phys. **140**, 074707 (2014).

[26] Y. Imaizumi, T. Omori, H. Kusudo, C. Bistafa, and Y. Yamaguchi, “Wilhelmy equation revisited: A lightweight method to measure liquid–vapor, solid–liquid, and solid–vapor interfacial tensions from a single molecular dynamics simulation,” J. Chem. Phys. **153**, 034701 (2020); arXiv:2004.14248.

[27] D. Surblys, Y. Yamaguchi, K. Kuroda, M. Kagawa, T. Nakajima, and H. Fujimura, “Molecular dynamics analysis on wetting and interfacial properties of water-alcohol mixture droplets on a solid surface,” J. Chem. Phys. **140**, 034505 (2014).

[28] Y. Yamaguchi, H. Kusudo, D. Surblys, T. Omori, and G. Kikugawa, “Interpretation of Young's equation for a liquid droplet on a flat and smooth solid surface: Mechanical and thermodynamic routes with a simple Lennard-Jones liquid,” J. Chem. Phys. **150**, 044701 (2019).

[29] H. Kusudo, T. Omori, and Y. Yamaguchi, “Extraction of the equilibrium pinning force on a contact line exerted from a wettability boundary of a solid surface through the connection between mechanical and thermodynamic routes,” J. Chem. Phys. **151**, 154501 (2019).

[30] F. Leroy, D. J. V. A. Dos Santos, and F. Müller-Plathe, “Interfacial excess free energies of solid-liquid interfaces by molecular dynamics simulation and thermodynamic integration,” Macromol. Rapid Commun. **30**, 864–870 (2009).

[31] F. Leroy and F. Müller-Plathe, “Solid-liquid surface free energy of Lennard-Jones liquid on smooth and rough surfaces computed by molecular dynamics using the phantom-wall method,” J. Chem. Phys. **133**, 044110 (2010).

[32] F. Leroy and F. Müller-Plathe, “Dry-surface simulation method for the determination of the work of adhesion of solid–liquid interfaces,” Langmuir **31**, 8335–8345 (2015).

[33] M. Kanduč and R. R. Netz, “Atomistic simulations of wetting properties and water films on hydrophilic surfaces,” J. Chem. Phys. **146**, 164705 (2017).

[34] M. Kanduč, “Going beyond the standard line tension: Size-dependent contact angles of water nanodroplets,” J. Chem. Phys. **147**, 174701 (2017).

[35] D. Surblys, F. Leroy, Y. Yamaguchi, and F. Müller-Plathe, “Molecular dynamics analysis of the influence of Coulomb and van der Waals interactions on the work of adhesion at the solid-liquid interface,” J. Chem. Phys. **148**, 134707 (2018).

[36] C. Bistafa, D. Surblys, H. Kusudo, and Y. Yamaguchi, “Water on hydroxylated silica surfaces: Work of adhesion, interfacial entropy, and droplet wetting,” J. Chem. Phys. **155**, 064703 (2021).

[37] E. M. Grzelak and J. R. Errington, “Computation of interfacial properties via grand canonical transition matrix Monte Carlo simulation,” J. Chem. Phys. **128**, 014710 (2008).

[38] G. V. Lau, I. J. Ford, P. A. Hunt, E. A. Müller, and G. Jackson, “Surface thermodynamics of planar, cylindrical, and spherical vapour-liquid interfaces of water,” J. Chem. Phys. **142**, 114701 (2015).

[39] V. Kumar and J. R. Errington, “The use of Monte Carlo simulation to obtain the wetting properties of water,” Phys. Procedia **53**, 44–49 (2014).

[40] V. R. Ardham, G. Deichmann, N. F. A. van der Vegt, and F. Leroy, “Solid-liquid work of adhesion of coarse-grained models of n-hexane on graphene layers derived from the conditional reversible work method,” J. Chem. Phys. **143**, 243135 (2015).

[41] H. Jiang, F. Müller-Plathe, and A. Z. Panagiotopoulos, “Going beyond the standard line tension: Size-dependent contact angles of water nanodroplets,” J. Chem. Phys. **147**, 084708 (2017).

[42] S. Ravipati, B. Aymard, S. Kalliadasis, and A. Galindo, “On the equilibrium contact angle of sessile liquid drops from molecular dynamics simulations,” J. Chem. Phys. **148**, 164704 (2018).

[43] T. Omori, Y. Kobayashi, Y. Yamaguchi, and T. Kajishima, “Understanding the asymmetry between advancing and receding microscopic contact angles,” Soft Matter **15**, 3923–3928 (2019).

[44] R. Bey, B. Coasne, and C. Picard, “Probing the concept of line tension down to the nanoscale,” J. Chem. Phys. **152**, 094707 (2020).

[45] J. H. Weijs, B. Andreotti, and J. H. Snoeijer, “Elasto-capillarity at the nanoscale: On the coupling between elasticity and surface energy in soft solids,” Soft Matter **9**, 8494 (2013).

[46] J.-C. Fernandez-Toledano, T. D. Blake, P. Lambert, and J. De Coninck, “On the cohesion of fluids and their adhesion to solids: Young's equation at the atomic scale,” Adv. Colloid Interface Sci. **245**, 102–107 (2017).

[47] J. Fan, J. De Coninck, H. Wu, and F. Wang, “Microscopic origin of capillary force balance at contact line,” Phys. Rev. Lett. **124**, 125502 (2020).

[48] J. Fan, J. De Coninck, H. Wu, and F. Wang, “A generalized examination of capillary force balance at contact line: On rough surfaces or in two-liquid systems,” J. Colloid Interface Sci. **585**, 320–327 (2021).

[49] H. Teshima, H. Kusudo, C. Bistafa, and Y. Yamaguchi, “Quantifying interfacial tensions of surface nanobubbles: How far can Young's equation explain?,” Nanoscale (to be published).

[50] A. V. Rode, S. T. Hyde, E. G. Gamaly, R. G. Elliman, D. R. McKenzie, and S. Bulcock, “Structural analysis of a carbon foam formed by high pulse-rate laser ablation,” Appl. Phys. A: Mater. Sci. Process. **69**, S755–S758 (1999).

[51] K. Falk, N. Fillot, A.-M. Sfarghiu, Y. Berthier, and C. Loison, "Interleaflet sliding in lipidic bilayers under shear flow: Comparison of the gel and fluid phases using reversed non-equilibrium molecular dynamics simulations," Phys. Chem. Chem. Phys. **16**, 2154–2166 (2014).

[52] Y. Homma, S. Chiashi, T. Yamamoto, K. Kono, D. Matsumoto, J. Shitaba, and S. Sato, "Photoluminescence measurements and molecular dynamics simulations of water adsorption on the hydrophobic surface of a carbon nanotube in water vapor," Phys. Rev. Lett. **110**, 157402 (2013).

[53] K. Imadate and K. Hirahara, "Experimental determination of the diameter-dependent wettability of carbon nanotubes as studied using atomic force microscopy," Phys. Chem. Chem. Phys. **20**, 26979–26985 (2018).

[54] R. C. Tolman, "The effect of droplet size on surface tension," J. Chem. Phys. **17**, 333–337 (1949).

[55] E. M. Blokhuis and J. Kuipers, "Thermodynamic expressions for the Tolman length," J. Chem. Phys. **124**, 074701 (2006).

[56] S. Tumram, K. Kesava Rao, and M. S. Ananth, "Augmented Gibbs–Tolman model for surface tension," Langmuir **33**, 11687–11697 (2017).

[57] J. A. W. Elliott, "Surface thermodynamics at the nanoscale," J. Chem. Phys. **154**, 190901 (2021).

[58] H. Yaguchi, T. Yano, and S. Fujikawa, "Molecular dynamics study of vapor-liquid equilibrium state of an argon nanodroplet and its vapor," J. Fluid Sci. Technol. **5**, 180 (2010).

[59] S. K. Das and K. Binder, "Universal critical behavior of curvature-dependent interfacial tension," Phys. Rev. Lett. **107**, 235702 (2011).

[60] B. Cheng and M. Ceriotti, "Communication: Computing the Tolman length for solid-liquid interfaces," J. Chem. Phys. **148**, 231102 (2018).

[61] P. Rehner and J. Gross, "Surface tension of droplets and Tolman lengths of real substances and mixtures from density functional theory," J. Chem. Phys. **148**, 164703 (2018).

[62] Y. Gao, K. Wu, Z. Chen, W. Tian, J. Li, Z. Huang, and J. Bi, "Model for interfacial tension of nanoconfined Lennard-Jones fluid," Energy Fuels **35**, 4044–4052 (2021).

[63] P. Montero de Hijes, J. R. Espinosa, E. Sanz, and C. Vega, "Interfacial free energy of a liquid-solid interface: Its change with curvature," J. Chem. Phys. **151**, 144501 (2019).

[64] S. Plimpton, "Fast parallel algorithms for short-range molecular dynamics," J. Comput. Phys. **117**, 1–19 (1995).

[65] B. Hess *et al.*, "GROMACS 4: Algorithms for highly efficient, load-balanced, and scalable–molecular simulation," J. Chem. Theory Comput. **4**, 435–447 (2008).

[66] S. M. Thompson, K. E. Gubbins, J. P. R. B. Walton, R. A. R. Chantry, and J. S. Rowlinson, "A molecular dynamics study of liquid drops," J. Chem. Phys. **81**, 530–542 (1984).

[67] C. Ma, C. Chen, Z. Xu, C. Lv, and Q. Zheng, "Substrate curvature dependence of intrinsic contact angles," Extreme Mech. Lett. **48**, 101388 (2021).

[68] H. Kusudo, T. Omori, and Y. Yamaguchi, "Local stress tensor calculation by the method-of-plane in microscopic systems with macroscopic flow: A formulation based on the velocity distribution function," J. Chem. Phys. **155**, 184103 (2021).

[69] E. A. Mastny and J. J. de Pablo, "Melting line of the Lennard-Jones system, infinite size, and full potential," J. Chem. Phys. **127**, 104504 (2007).

[70] S. Chiashi, Y. Saito, T. Kato, S. Konabe, S. Okada, T. Yamamoto, and Y. Homma, "Confinement effect of sub-nanometer difference on melting point of ice-nanotubes measured by photoluminescence spectroscopy," ACS Nano **13**, 1177–1182 (2019).